

1 **Estimating the impact of a major hurricane on**
2 **transport processes**

3 Thomas Dobbelaere, Emmanuel Hanert

4 February 17, 2021

5 **Abstract**

6 In most hydrodynamic model studies, currents and waves are simu-
7 lated separately. This is especially true for the simulation of passive
8 drifters, whose trajectories are often computed based solely on cur-
9 rents. Although this simplification holds for most situations, as the
10 force exerted by waves on currents can be neglected in fair weather
11 conditions, it may lead to significant errors in storm conditions, during
12 which local currents are strongly influenced by wind-generated waves.
13 In this study, current-wave interactions in heavy-wind conditions are
14 studied by coupling the unstructured-mesh hydrodynamic model SLIM
15 with the wave model SWAN in the Florida Reef Tract during Hurricane
16 Irma (Sep. 2017). This coupled model successfully reproduced both
17 the observed wave behavior and storm surge during the hurricane.
18 The modeled currents were then used to simulate the trajectories of
19 passive drifters during the passage of the hurricane. Our results show
20 that taking wave force into account induces variations of up 1 m/s in
21 modelled currents on the continental shelf break as well as in the vicin-
22 ity of reefs and islands. Wave-current interactions can therefore deflect
23 the trajectories of drifting material by up to 10 km on the passage of
24 the storm **Add something?**. These results strongly advocate for the
25 inclusion of wave forces while studying transport processes (sediments,
26 pollutants, larvae, etc.) under storm conditions

²⁷ **1 Introduction**

²⁸ Wave-current interactions in coastal areas are of great importance for coastal
²⁹ engineering as they play a key role in sediment transport, morphological
³⁰ evolution and pollutant mixing (Bever and MacWilliams, 2013; Li and Johns,
³¹ 1998). However, these interactions are highly nonlinear and can vary sig-
³² nificantly in space and time (Wu et al., 2011). Wave-induced currents are
³³ generated by wave radiation gradients (Longuet-Higgins, 1970), affecting
³⁴ water levels near shorelines and wave breaking points (Longuet-Higgins and
³⁵ Stewart, 1964), while changes in water levels and currents, in turn, affect the
³⁶ motion and evolution of waves (Sikirić et al., 2013). Coupled wave-current
³⁷ models are therefore required to capture these complex interactions.

³⁸ As coastal oceans are characterized by local complex geometries with
³⁹ islands, inlets and estuaries, unstructured (usually two-dimensional) mod-
⁴⁰ els are preferred as structured grid models show limitations in resolving
⁴¹ topologically controlled nearshore processes (Wu et al., 2011; Chen et al.,
⁴² 2007). The effect of wave-interactions becomes even more significant in
⁴³ the case of hurricanes, that generate large wind-waves and disturb ocean
⁴⁴ conditions (Liu et al., 2020) by causing coastal upwellings on continental
⁴⁵ shelves (Smith, 1982) and inducing strong currents, waves and storm surges
⁴⁶ in nearshore and coastal regions (Dietrich et al., 2010; Weisberg and Zheng,
⁴⁷ 2006). South Florida and the Gulf of Mexico are particularly vulnerable to
⁴⁸ hurricanes (Malmstadt et al., 2009) and modelling studies predict tropical
⁴⁹ cyclones to increase both in frequency and intensity in this region (Mar-
⁵⁰ sooli et al., 2019; Knutson et al., 2010). Being able to accurately model
⁵¹ wave-current interactions in this area becomes thus critical.

⁵² Individual-based modelling of particulates has been extensively used to
⁵³ study the transport of drifting materials such as pollutants, sediments or
⁵⁴ larvae (Garcia-Pineda et al., 2020; Liubartseva et al., 2018; Figueiredo et al.,
⁵⁵ 2013; Frys et al., 2020). Although some of these studies take the impact
⁵⁶ of waves into account by adding Stokes drift velocity, *i.e.* the net drift of a
⁵⁷ floating particle in the direction of the wave propagation (Van Den Bremer
⁵⁸ and Breivik, 2018), to the Eulerian currents, they usually neglect the wave-
⁵⁹ induced currents. Such practice is reasonable in the case of fair weather,
⁶⁰ when wave-induced forces exerted on currents are relatively smaller, but

61 might lead to significant inaccuracies during storm conditions. To assess
62 the importance of wave-current interactions during a tropical cyclone, we
63 investigated the transport of drifting particulates on the Florida shelf during
64 Hurricane Irma, one of the strongest and costliest tropical cyclones on
65 records in the Atlantic Basin (Chen et al., 2007), that made landfall in Florida
66 in September 2017.

67 In this study, we developed an unstructured coupled wave-current model of
68 South Florida to simulate the ocean circulation during hurricane Irma. Both
69 modelled currents and waves were validated against field measurements
70 and were then used to simulate the transport of drifting material in the
71 Florida Keys and the Florida inner shelf during the storm. Model outputs
72 were then compared with uncoupled simulation results in order to assess
73 the impact of wave-induced forces and Stokes drift on the modelled currents
74 and transports.

75 **2 Methods**

76 **2.1 Study area and data**

77 Large-scale ocean circulation around South Florida is dominated by the
78 Florida Current (FC), which originates from the Loop Currents (LC) where it
79 enters the Florida Straits from the Gulf of Mexico, and, downstream, forms
80 the Gulf Stream. The FC is a major western boundary current character-
81 ized by spatial variability and meandering, associated with the presence
82 of cyclonic eddies between the core of the current and the complex reef
83 topography of the Florida Reef Tract (FRT) (Lee et al., 1995; Kourafalou and
84 Kang, 2012). The northern half of these reefs are made of early Holocene
85 reef frameworks and indurated sand ridges while the southern part (the
86 Florida Keys) is composed of a chain of limestone islands, fossilized rem-
87 nants of ancient coral reefs and sand bars (Hoffmeister and Multer, 1968;
88 Shinn, 1988; Lidz and Shinn, 1991). The variability of the FC extends over
89 a large range of spatial and temporal scales, with periods of 30-70 days in
90 the Lower Keys (Lee et al., 1995) and shorter periods of 2-21 days in the
91 Upper Keys (Lee and Mayer, 1977), and exhibits significant seasonal and
92 interannual cycles (Johns and Schott, 1987; Lee and Williams, 1988; Schott

93 et al., 1988). Circulation on the West Florida Shelf (WFS) on the other hand
94 is forced by local winds and tidal fluctuations (Lee and Smith, 2002; Liu and
95 Weisberg, 2012).

96 Field observations were used to validate our model outputs. Modelled sea
97 surface elevation was validated against tide gauge measurements from
98 the National Oceanic and Atmospheric Administrations (NOAA) Tides and
99 Currents dataset. These measurements were taken at four locations: two
100 in the Florida Keys (Key West and Vaca Key); one on the eastern coast
101 of Florida (Key West); and one on the western coast (Naples). Currents
102 were validated against ADCP measurements from the University of South
103 Florida's College of Marine Science's (USF/CMS) Coastal Ocean Monitoring
104 and Prediction System (COMPS) for the WFS (Weisberg et al., 2009). More
105 specifically, we used measurements from moorings C10, C12 and C13,
106 respectively located at the 25, 50, and 50 m isobaths of the WFS (Liu
107 et al., 2020). Finally, validation of modelled wave parameters was performed
108 against four buoy measurements from NOAA's National Data Buoy Center
109 (NDBC): two on Florida's Eastern shelf and two on the WFS. The locations
110 of all measurement stations are shown on Fig. 1

111 **2.2 Wind and atmospheric pressure for Hurricane Irma**

112 Irma made landfall in Florida on 10 September 2017 as a category 3 storm,
113 first at Cudjoe Key (Florida Keys) and later on Marco Island, south to Naples
114 (see hurricane track in Fig. 1). It then weakened to a category 2 storm as it
115 moved further inland (Pinelli et al., 2018). The storm caused damages to
116 up to 75% of the buildings at his landfall point in the Florida Keys, making
117 it one of the strongest and costliest hurricanes on record in the Atlantic
118 basin (Xian et al., 2018; Zhang et al., 2019). The strongest reported wind
119 speed was 50 m/s on Marco Island while the highest recorded storm surge
120 was 2.3 m, although larger wind speed likely occurred in the Florida Keys
121 (Pinelli et al., 2018) In order to reproduce the wind profile of Irma in our
122 model, high-resolution H*Wind (Powell et al., 1998) wind fields were used.
123 As these data represent 1-min averaged wind speeds, we multiplied them by
124 a factor 0.93 to obtain 10-min averaged wind speeds (Harper et al., 2010),
125 more consistent with the time step of our model. Furthermore, H*Wind

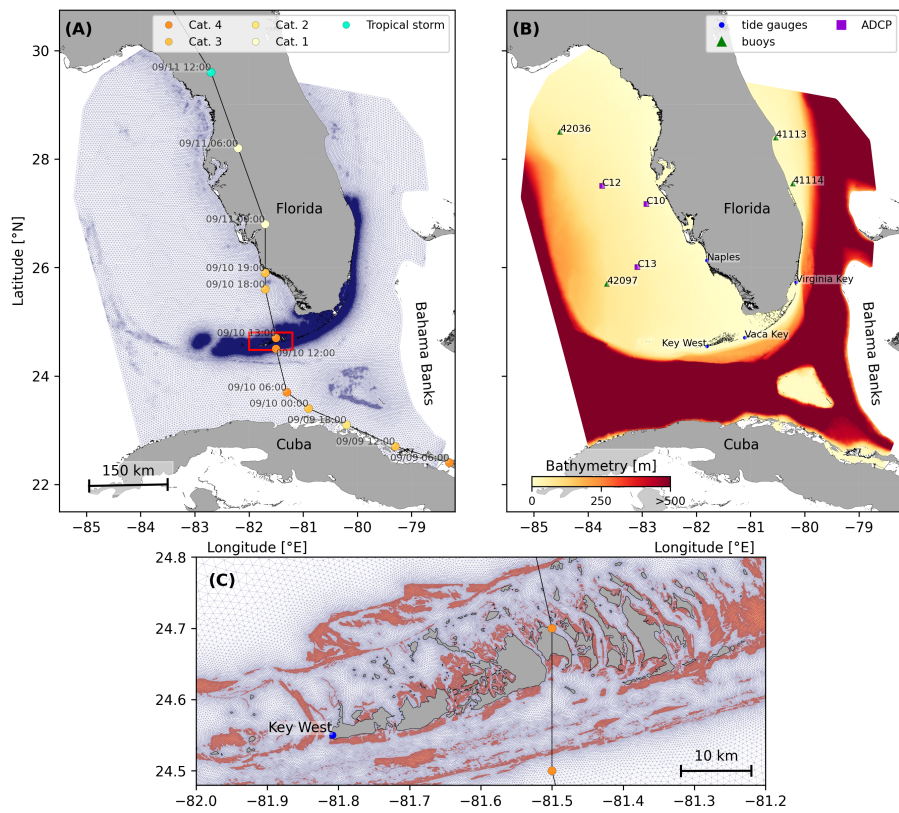


Fig. 1: **(A)** Mesh of the computational domain with the trajectory of Irma, category of the hurricane is given by the Saffir-Simpson color scale. **(B)** Bathymetry of the domain with the location of stations used for the validation of the model outputs. **(C)** Close up view of the Lower Keys area, where the mesh resolution reaches 100m near reefs (shown in coral) and islands (highlighted in dark grey)

126 wind profiles did not cover the whole model extent during the hurricane and
 127 were thus blended within coarser wind field extracted from ECMWF ERA-5
 128 datasets. Pressure fields of Irma were also constructed using ERA-5 data.
 129 However, the coarse resolution of the data set caused the depression at the
 130 center of the hurricane to get smoothed out, leading to an underestimation of
 131 the pressure gradient in our model. To better capture the central depression
 132 of Irma, we built a hybrid pressure field using the position and the minimal
 133 pressure of the core of the hurricane based on its track in the HURDAT
 134 2 database (Landsea and Franklin, 2013). Based on this information, the
 135 hybrid pressure field was constructed by combining an idealized Holland
 136 pressure profile (Lin and Chavas, 2012) within the radius of maximum
 137 wind speed of Irma (Knaff et al., 2018) with ERA-5 pressure field. The
 138 transition between from the Holland profile to ERA-5 data outside the radius
 139 of maximum wind speed data was performed using a smooth step function.

140 **2.3 Hydrodynamic model**

141 Ocean currents generated during hurricane Irma around South Florida were
 142 modelled using the 2D barotropic version of the unstructured-mesh coastal
 143 ocean model SLIM¹. The model mesh covers an area similar to the model
 144 extent of Dobbelaere et al. (2020b), that includes the FRT but also the
 145 Florida Strait and part of the Gulf of Mexico (Figure 1). However, this area
 146 has been slightly extended northeastward and westward in order to include
 147 the NOAA-NDBC buoys. Furthermore, in order to withstand potential cell
 148 drying due to storm conditions in this study, we solved the conservative
 149 shallow water equations with wetting-drying, that write:

$$\begin{aligned}
 \frac{\partial H}{\partial t} + \nabla \cdot (\mathbf{U}) &= 0 \\
 \frac{\partial \mathbf{U}}{\partial t} + \nabla \cdot \left(\frac{\mathbf{U}\mathbf{U}}{H} \right) &= -f \mathbf{e}_z \times \mathbf{U} + \alpha g H \nabla(H - h) - \frac{1}{\rho} \nabla p_{\text{atm}} + \frac{1}{\rho} \boldsymbol{\tau}_s \quad (1) \\
 &\quad + \nabla \cdot (\nu \nabla \mathbf{U}) - \frac{C_b}{H^2} |\mathbf{U}| \mathbf{U} + \gamma (\mathbf{U}_* - \mathbf{U})
 \end{aligned}$$

150 where H is the water column height and \mathbf{U} is the depth-averaged transport;
 151 f is the Coriolis coefficient; g is the gravitational acceleration; h is the

¹<https://www.slim-ocean.be>

152 bathymetry; α is a coefficient stating whether the mesh element is wet
 153 ($\alpha = 1$) or dry ($\alpha = 0$); ν is the viscosity; C_b is the bulk bottom drag
 154 coefficient; ∇p_{atm} is the atmospheric pressure gradient; τ_s is the surface
 155 stress due to wind; and γ is a relaxation coefficient towards a reference
 156 transport U_* . As in Frys et al. (2020) and Dobbelaere et al. (2020b), SLIM
 157 currents were gradually relaxed towards HYCOM (Chassignet et al., 2007) in
 158 regions where the water depth exceeds 50m.

159 At very high wind speeds, the white cap is blown off the crest of the waves,
 160 which generates a layer of droplets that acts as a slip layer for the winds
 161 at the ocean-atmosphere interface (Holthuijsen et al., 2012). This causes
 162 a saturation of the wind drag coefficient for strong winds (Donelan et al.,
 163 2004; Powell et al., 2003). To account for the impact of this saturation
 164 on the surface wind stress in our model, we implemented the wind drag
 165 parameterization of Moon et al. (2007). In this parameterization, the drag
 166 coefficient C_d depends on the wind speed at 10-m height U_{10} according to:

$$C_d = \kappa^2 \log \left(\frac{10}{z_0} \right)^{-2} \quad (2)$$

167 where κ is the von Karman constant. The roughness length z_0 in Eq. 2 is a
 168 function of the 10-m wind speed U_{10} , whose expression writes:

$$z_0 = \begin{cases} \frac{0.0185}{g} U_*^2 & \text{if } U_{10} \leq 12.5 \text{ m/s} \\ [0.085(-0.56U_*^2 + 20.255U_* + 2.548) - 0.58] \times 10^{-3} & \text{if } U_{10} > 12.5 \text{ m/s} \end{cases} \quad (3)$$

169 with U_* the friction velocity. The relation between U_{10} and U_* is given by:

$$U_{10} = -0.56U_*^2 + 20.255U_* + 2.458 \quad (4)$$

170 The mesh resolution depended on the distance to coastlines and reefs,
 171 bathymetry and bathymetry gradient in order to satisfy SWAN refinement
 172 criterion $h/A \geq a$, where h is the water depth and A is the element area.
 173 The mesh was generated using the Python library seamsh², based on the
 174 the open-source mesh generator GMSH (Geuzaine and Remacle, 2009) and
 175 is composed of approximately 7.7×10^5 elements. The coarsest elements,

²<https://pypi.org/project/seamsh/>

¹⁷⁶ far away from the FRT, had a characteristic length size of about 5 km, as
¹⁷⁷ shown in Fig 1 along with the bathymetry of the model domain.

¹⁷⁸ **2.4 Wave model**

¹⁷⁹ Waves were modelled using parallel unstructured SWAN (Booij et al., 1999)
¹⁸⁰ on the same mesh as SLIM. This model solves the action balance equation,
¹⁸¹ which reads (Mei, 1989):

$$\frac{\partial N}{\partial t} + \nabla_x \cdot [(c_g + \mathbf{u})N] + \frac{\partial}{\partial \theta}[c_\theta N] + \frac{\partial}{\partial \sigma}[c_\sigma N] = \frac{S_{in} + S_{ds} + S_{nl}}{\sigma} \quad (5)$$

¹⁸² where $N = E/\sigma$ is the wave action density; θ is the wave propagation
¹⁸³ direction; σ is the wave relative frequency; c_g is the wave group velocity,
¹⁸⁴ $\mathbf{u} = \mathbf{U}/H$ is SLIM depth-averaged current velocity; c_θ and c_σ are the propa-
¹⁸⁵ gation velocities in spectral space due to refraction and shifting in frequency
¹⁸⁶ due to variations in depth and currents; and S_{in} , S_{ds} , and S_{nl} respectively
¹⁸⁷ represent wave growth by wind, wave decay and nonlinear transfers of
¹⁸⁸ wave energy through interactions between triplets and quadruplets. Spectra
¹⁸⁹ were discretized with 48 direction bins and 50 frequency bins logarithmically
¹⁹⁰ distributed from 0.3 to 2 Hz. Exponential wind growth was parameterized
¹⁹¹ using the formulation of Janssen (1991), while dissipations by whitecapping
¹⁹² and bottom dissipations followed the formulations of Komen et al. (1984)
¹⁹³ and Madsen et al. (1989) respectively. Coefficients for exponential wind
¹⁹⁴ growth and whitecapping parameterizations were based on the results of
¹⁹⁵ Siadatmousavi et al. (2011). [Insist that not the default parameterization].
¹⁹⁶ Finally, wave boundary conditions were derived from WAVEWATCH III (Tol-
¹⁹⁷ man et al., 2009) spectral outputs at buoy locations. TODO: more info on
¹⁹⁸ Stokes drift Depth-averaged Stokes drift was also computed by SWAN using
¹⁹⁹ the following formula:

$$\mathbf{u}_s = \int_0^{2\pi} \int_0^{+\infty} \frac{\sigma^3}{h \tanh(2kh)} E(\sigma, \theta) (\cos \theta, \sin \theta) d\sigma d\theta \quad (6)$$

²⁰⁰ where k is the norm of the wave vector; h is the water depth; and $E(\sigma, \theta)$ is
²⁰¹ the wave energy density.

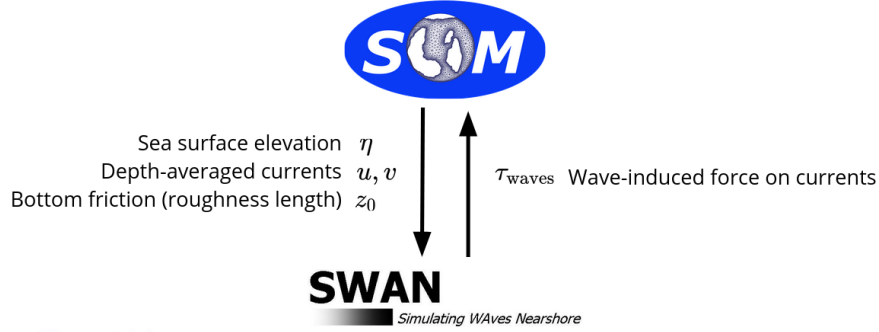


Fig. 2: Schematic illustration of the coupled SLIM+SWAN model.

202 2.5 Coupled model

203 SLIM and SWAN are coupled together such that they share information in
 204 both ways at each time step (Fig. 2). The two models are run consecutively
 205 at each time step. First, SLIM computes the sea surface elevation η and
 206 depth-averaged current velocity $\mathbf{u} = (u, v)$. These quantities are transferred
 207 to SWAN to update the model water depth as well as the second term of
 208 equation 5 governing wave energy propagation in the geographic space.
 209 Moreover, in order for the two model to have consistent bottom dissipa-
 210 tion parameterizations, SLIM bottom drag coefficient is transformed into a
 211 roughness length z_0 following the methodology of Dietrich et al. (2011). This
 212 roughness length is then converted into Madsen's bottom dissipation term
 213 in SWAN. SWAN then produces the wave-induced force on current τ_{wave}
 214 by computing the wave radiation stress gradient. This quantity is used to
 215 update the value of the surface stress τ_s in equation 1, that now becomes
 216 the sum of wind and wave-induced forces $\tau_s = \tau_{\text{wind}} + \tau_{\text{wave}}$. **TODO: Add**
 217 **some stuff**

218 3 Results

219 **Add short intro**

220 **3.1 Validation**

221 (reformulate sentence) Comparisons of H*Wind wind and hybrid pressure
222 fields with station measurements and ECMWF ERA-5 profiles at Vaca Key
223 station are shown in Fig. 3. The hybrid pressure field shows better agree-
224 ment with observations than ERA-5 pressure as it successfully reproduces
225 the storm depression. ERA-5 fields, on the other hand, fail to resolve the
226 low pressure at the core of the hurricane due to their coarser grid (TODO:
227 add how much). Both H*Wind and ERA-5 agree well with observed wind
228 speeds although both data sets tend to slightly overestimate the width and
229 intensity of the wind peak. However, H*wind profiles show a better match
230 with the timing of the observed peak, that ERA-5 winds tend to anticipate.
231 H*wind also exhibits a slightly narrower peak in wind speed, which better
232 agrees with observations.

233 Hydrodynamic outputs of the coupled wave-current agree well with tide
234 gauge and ADCP measurements (Fig. 4). The timing and amplitude of the
235 storm surges are well reproduced by the coupled model, the largest model
236 error being an overestimation of 18 cm of the elevation peak at Virginia Key.
237 The fit is especially good at Naples, where both the positive and negative
238 surges are captured by the coupled model with a 5 cm accuracy. This
239 result is of interest as negative surges, although less studied, affect water
240 exchanges between the estuaries and the coastal ocean and disturb the
241 benthic ecosystems (Liu et al., 2020). Modelled 2D currents were validated
242 against depth-averaged ADCP measurements at mooring station C10, C12
243 and C13 (4). As in (Liu et al., 2020), vector correlation analysis (Kundu,
244 1976) is performed to compare modelled and observed current velocity
245 vectors. Correlation coefficients (ρ) between simulated and observed depth-
246 averaged currents were 0.84, 0.74 and 0.73 respectively C10, C12 and
247 C13 locations respectively. Average veering angles were computed as
248 well and were below 12°, as in (Liu et al., 2020). However, in our case, no
249 clear overestimation of southward currents was observed during Irma. As
250 expected from a depth-averaged model, the best fit with observations is
251 obtained at the shallowest mooring C10, located on the 25m isobath, with
252 an average veering angle of 6°.

253 The simulated significant wave height agrees well with observations on the
254 WFS, where errors on the peak value do not exceed ??? %. On the East

Validation of atmospheric forcings at Vaca Key station

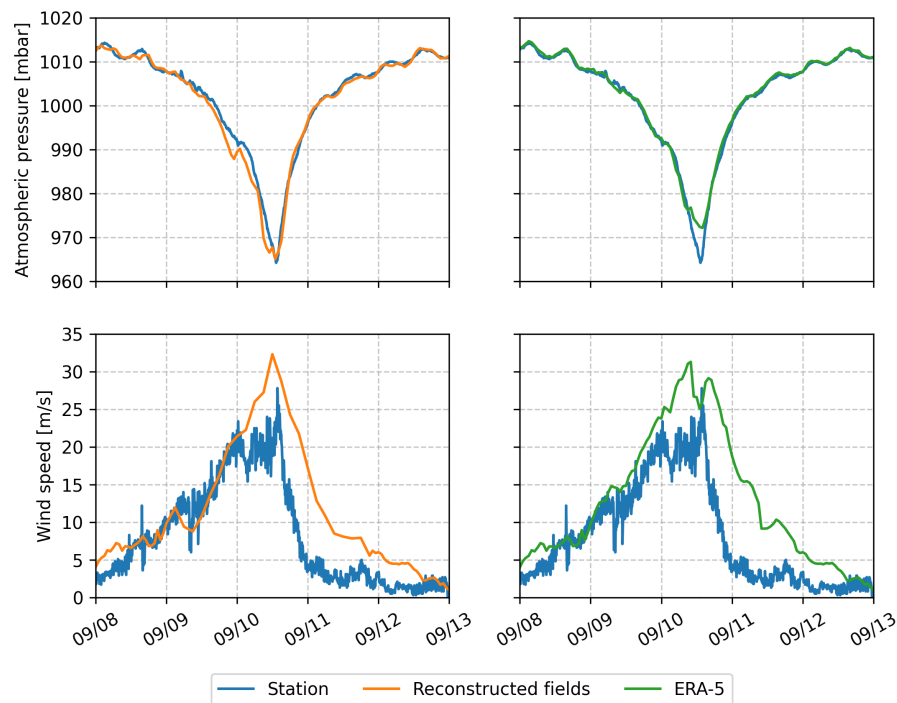


Fig. 3: Comparison of reconstructed wind atmospheric pressure with field measurements and coarser ECMWF ERA-5 profiles during Irma. The generated hybrid atmospheric better capture the observed storm depression while H*wind winds better match the measured peak in wind speed.

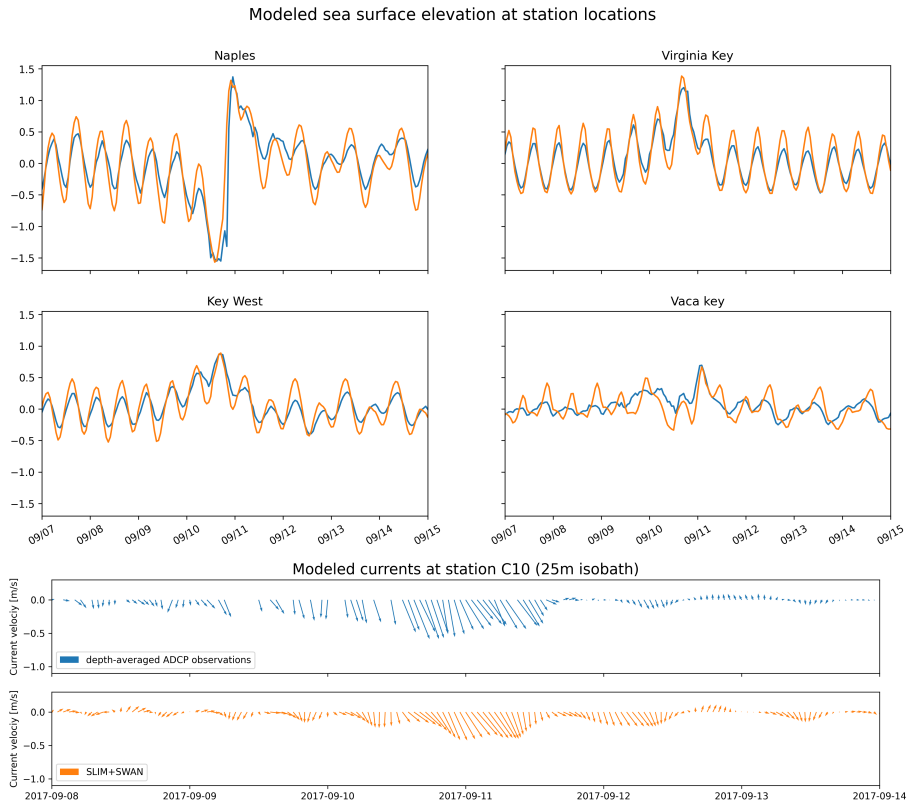


Fig. 4: Comparison of modelled sea surface elevation and current velocity with tide gauge measurements and observed velocity at mooring C10 (see Fig. 1 for their location). Timing and amplitudes of the storm surges are well reproduced by the model. Modelled current velocities agree well with observations, with a correlation coefficient of 0.83 and an average veering angle of 6° at mooring C10.

255 Florida Shelf, errors are slightly larger reaching ??? %. Although the model
256 outputs agree well with observations, a lag in significant wave height is
257 observed for all 4 buoys. Moreover, the peak in significant wave height
258 tends to be underestimated at buoys 41113 and 41114, located on the East
259 Florida Shelf. Other wave parameters were better reproduced by the model
260 on the WFS as well, as illustrated for buoy 42036 in Fig. 5. This good
261 fit on the WFS is not surprising as the parameters used for wing energy
262 input and whitecapping dissipation were based on the calibration performed
263 by (Siadatmousavi et al., 2011) on the Northern Gulf of Mexico. Wind-
264 induced wave growth might therefore be underestimated on the eastern
265 shelf. Consequently, incident wave do not receive enough energy to grow
266 after breaking on the bank boundary, leading to an underestimation of the
267 significant wave height at the location of the buoys. Nonetheless, as this
268 study focused on the wave produced by Irma , that made landfall on the
269 western coasts of Florida, the use of parameterizations calibrated for the
270 Gulf of Mexico seems reasonable.

271 **3.2 Impact of waves on currents and transport**

272 The impact of hurricane-induced wave-current interactions is first evaluated
273 by computing the norm of the maximum difference in current velocity be-
274 tween uncoupled SLIM and coupled SLIM+SWAN model runs during the
275 passage of Irma through the Florida Keys (from 2017-09-07 to 2017-09-13).
276 The differences in modelled currents appear to be stronger on the shelf
277 break and over coral reefs (Fig. 6). These results highlight the significant
278 impact of wave-induced forces, that can yield differences of up to 1 m/s dur-
279 ing the hurricane, with stronger currents being obtained with SLIM+SWAN.
280 This suggests that neglecting wave-current interactions during Irma would
281 results in a significant underestimation of transport over reefs.
282 To quantify the impact of these differences in velocity fields, we compared
283 the trajectories of virtual particles driven by currents produced by SLIM
284 alone and SLIM+SWAN simulations in the Florida Keys. First, we identified
285 the areas where the differences between the modelled currents were the
286 largest. Then, we determined the potential origination regions of particles
287 reaching these areas on the passage of the hurricane through the Florida

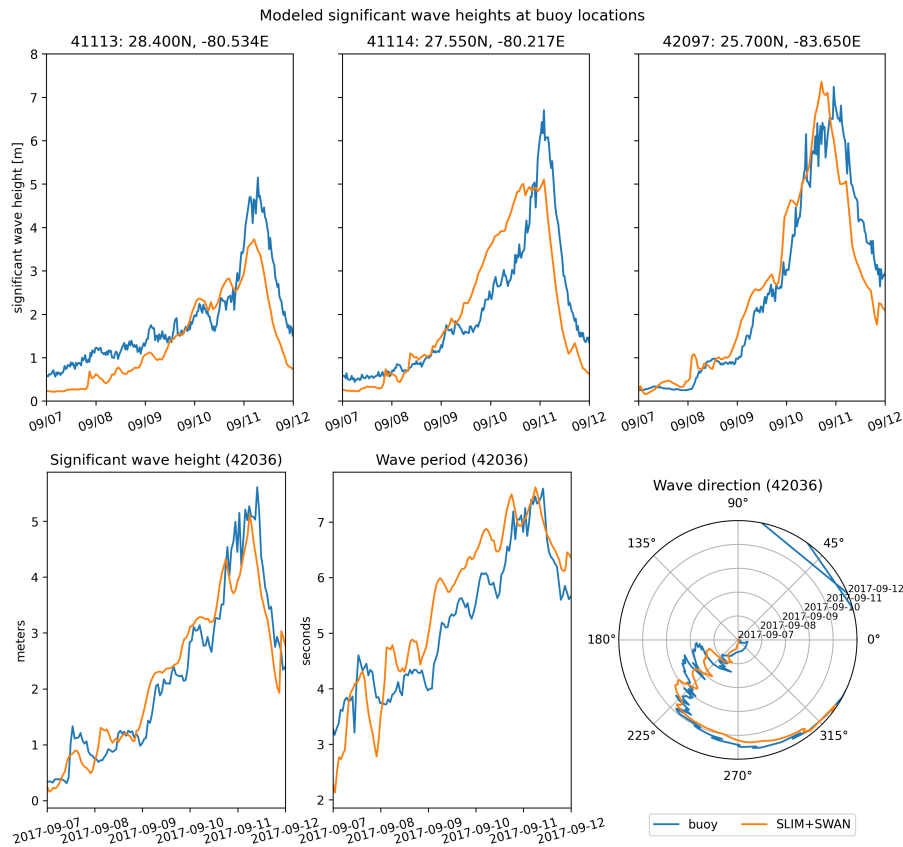


Fig. 5: Comparison of modelled wave parameters with observation at buoys location. Modelled significant wave height agrees well with field measurement. As model parameters were calibrated for the Northern Gulf of Mexico, observations are better reproduced at buoys located on the WFS, as illustrated for buoy 42036

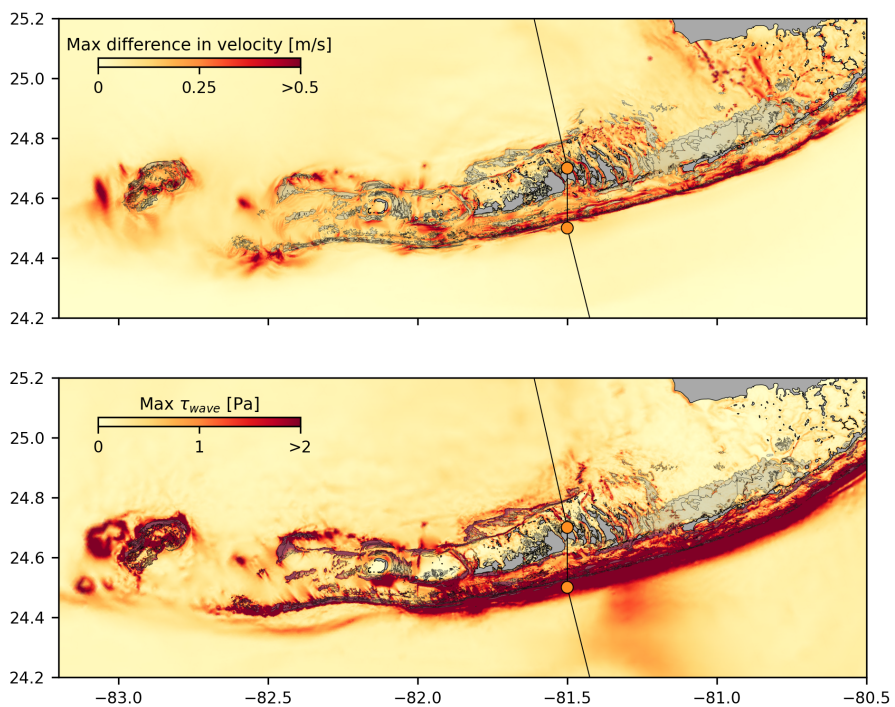


Fig. 6: Maximum of the difference between SLIM and SLIM+SWAN currents speed between 2017-09-07 00:00:00 and 2017-09-13 00:00:00. The difference between the coupled and uncoupled model, which represents the effect of the wave-induced stress, can yield differences of 0.5 m/s in the simulated currents during the passage of the hurricane. SLIM+SWAN currents velocities are larger than the currents modeled by SLIM alone. Islands are highlighted in dark grey and coral reefs in lighter grey

288 Keys using backtracking methods (Dobbelere et al., 2020a). These regions
289 are highlighted by the 4 release regions of Fig. 7. Finally, particles were
290 released from these four regions and advected by currents produced by the
291 coupled and uncoupled models. At each time step, the center of mass of
292 the modelled particle clouds were computed. The distance between these
293 centers of mass was used as a measure of the impact of the wind-generated
294 wave coupling on the modelled current in the Florida Keys during hurricane
295 Irma. This comparison was performed with 3 sets of currents: the currents
296 modelled by uncoupled SLIM (SLIM); the currents modelled by coupled
297 SLIM+SWAN (SLIM+SWAN); and the SLIM+SWAN currents with depth-
298 averaged Stokes drift (SLIM+SWAN+Stokes) [sentence is too condensed].
299 The results of these comparisons are shown in Fig. 7 [reformulate as active
300 sentence]. Differences between the modelled trajectories are negligible
301 before the passage of the hurricanes in the Florida Keys. Then, distance
302 between the centers of mass of the particles abruptly increase to up to
303 tens of kilometers as Irma gets through the Keys to finally stabilize after
304 the passage of the hurricane. These results support the assumption that
305 wave-induced transport is negligible compared to advection by Eulerian
306 currents in fair weather conditions. Particles advected by the currents of
307 the coupled model tend to remain on the shelf while particles advected by
308 SLIM alone are mostly transported along the shelf break. Although not
309 shown in this paper, comparison of SLIM and SLIM+SWAN trajectories were
310 conducted as well. The evolution of the distance between centers of mass
311 of the particle clouds showed similar trends while yielding smaller values.
312 Modelled maximal depth-averaged Stokes drift reached up to 0.2 m/s during
313 the passage of Irma through the Florida Keys. This suggests that both the
314 impact of wave-induced force on Eulerian currents and Stokes drift should be
315 taken into account while modelling particle transport under storm conditions.

316 4 Discussion and conclusions

317 Impact of waves on coral connectivity
318 Ability of wave model to correctly capture gradient in significant wave height
319 due to current-waves interactions under tropical cyclones depends on:

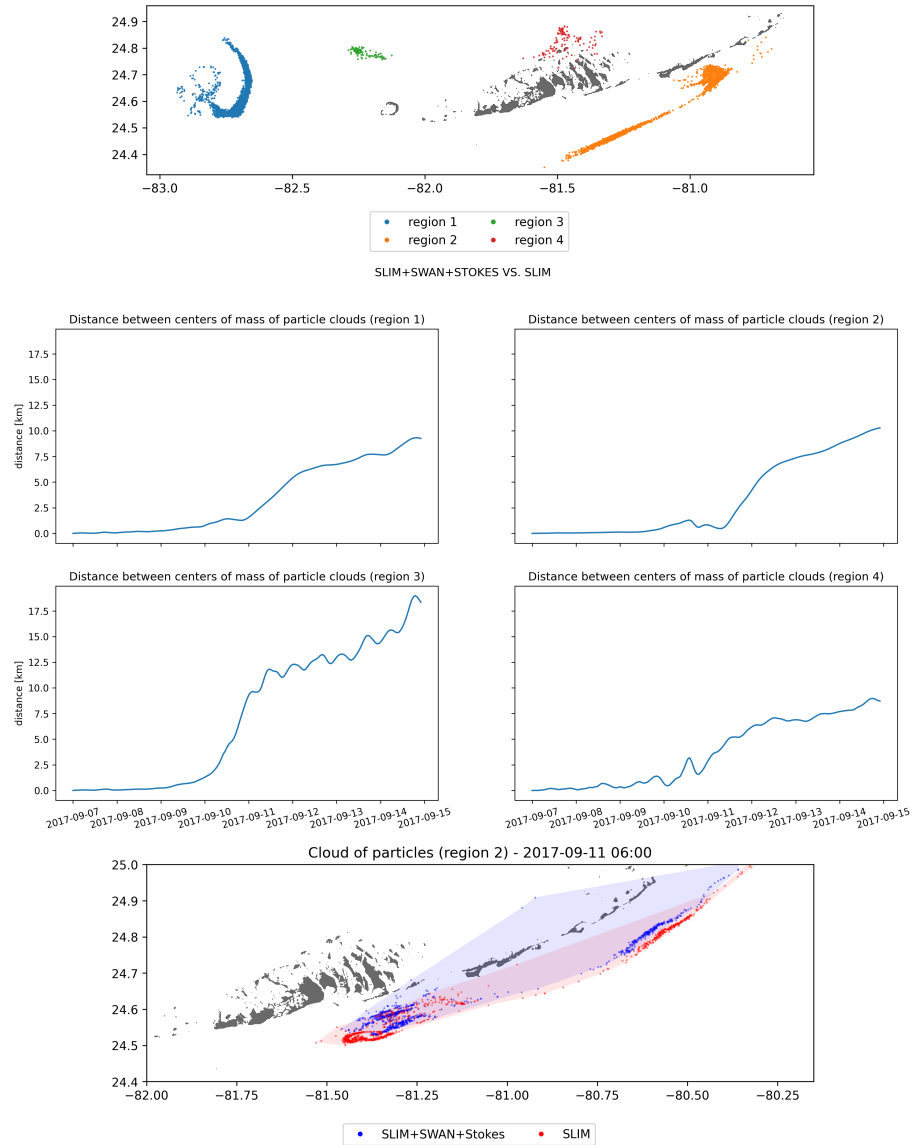


Fig. 7: Comparison of passive drifters trajectories with SLIM+SWAN+Stokes drift vs. SLIM alone. A snapshot of the positions of the particles released from region 2 is shown after the passage of Irma in the Florida Keys. Particles advected by the currents of the coupled model tend to remain on the shelf while particles advected by SLIM alone are mostly transported along the shelf break

- 320 • Broad perspective \Rightarrow not limited to FL
- 321 • Mention search and rescue
- 322 • However, ignoring waves in storm conditions could result in significant
323 inaccuracies in modelled trajectories, as illustrated in the case of
324 release region 2 in Fig. 7
- 325 • Spatial (10km \rightarrow 5km) and spectral (36 dir. \rightarrow 48 dir.) resolution
326 (Hegermiller et al., 2019)
- 327 • Directional spreading of incident waves (Villas Bôas et al., 2020)

328 **Conflict of Interest Statement**

329 The authors declare that the research was conducted in the absence of any
330 commercial or financial relationships that could be construed as a potential
331 conflict of interest.

332 **Author Contributions**

333 **Funding**

334 **Acknowledgments**

335 Computational resources were provided by the Consortium des Équipements
336 de Calcul Intensif (CÉCI), funded by the F.R.S.-FNRS under Grant No. 2.5020.11.
337 Thomas Dobbelaere is a PhD student supported by the Fund for Research
338 training in Industry and Agriculture (FRIA/FNRS).

339 **Supplementary Material**

340 The Supplementary Material for this article is attached to the submitted
341 document.

342 **References**

- 343 Bever, A. J. and MacWilliams, M. L. (2013). Simulating sediment transport
344 processes in San Pablo Bay using coupled hydrodynamic, wave, and
345 sediment transport models. *Marine Geology*, 345:235–253.
- 346 Booij, N., Ris, R. C., and Holthuijsen, L. H. (1999). A third-generation wave
347 model for coastal regions: 1. Model description and validation. *Journal*
348 of *geophysical research: Oceans*, 104(C4):7649–7666.
- 349 Chassignet, E. P., Hurlburt, H. E., Smedstad, O. M., Halliwell, G. R., Hogan,
350 P. J., Wallcraft, A. J., Baraille, R., and Bleck, R. (2007). The HYCOM
351 (hybrid coordinate ocean model) data assimilative system. *Journal of*
352 *Marine Systems*, 65(1-4):60–83.
- 353 Chen, C., Huang, H., Beardsley, R. C., Liu, H., Xu, Q., and Cowles, G. (2007).
354 A finite volume numerical approach for coastal ocean circulation studies:
355 Comparisons with finite difference models. *Journal of Geophysical*
356 *Research: Oceans*, 112(C3).
- 357 Dietrich, J., Bunya, S., Westerink, J., Ebersole, B., Smith, J., Atkinson,
358 J., Jensen, R., Resio, D., Luettich, R., Dawson, C., et al. (2010). A
359 high-resolution coupled riverine flow, tide, wind, wind wave, and storm
360 surge model for southern Louisiana and Mississippi. part ii: Synoptic
361 description and analysis of hurricanes Katrina and Rita. *Monthly Weather*
362 *Review*, 138(2):378–404.
- 363 Dietrich, J., Westerink, J., Kennedy, A., Smith, J., Jensen, R., Zijlema, M.,
364 Holthuijsen, L., Dawson, C., Luettich, R., Powell, M., et al. (2011).
365 Hurricane Gustav (2008) waves and storm surge: Hindcast, synoptic
366 analysis, and validation in southern Louisiana. *Monthly Weather Review*,
367 139(8):2488–2522.
- 368 Dobbelaere, T., Muller, E., Gramer, L., Holstein, D., and Hanert, E. (2020a).
369 Report on the potential origin of the SCTLD in the Florida Reef Tract.
370 Available online at: <https://floridadep.gov/rcp/coral/documents/report-potential-origin-sctld-florida-reef-tract>.
- 372 Dobbelaere, T., Muller, E. M., Gramer, L. J., Holstein, D. M., and Hanert, E.
373 (2020b). Coupled epidemic-hydrodynamic modeling to understand the

- 374 spread of a deadly coral disease in Florida. *Frontiers in Marine Science*,
375 7:1016.
- 376 Donelan, M., Haus, B., Reul, N., Plant, W., Stiassnie, M., Gruber, H., Brown,
377 O., and Saltzman, E. (2004). On the limiting aerodynamic roughness of
378 the ocean in very strong winds. *Geophysical Research Letters*, 31(18).
- 379 Figueiredo, J., Baird, A. H., and Connolly, S. R. (2013). Synthesizing larval
380 competence dynamics and reef-scale retention reveals a high potential
381 for self-recruitment in corals. *Ecology*, 94(3):650–659.
- 382 Frys, C., Saint-Amand, A., Le Hénaff, M., Figueiredo, J., Kuba, A., Walker, B.,
383 Lambrechts, J., Vallaeyns, V., Vincent, D., and Hanert, E. (2020). Fine-
384 scale coral connectivity pathways in the Florida Reef Tract: implications
385 for conservation and restoration. *Frontiers in Marine Science*, 7:312.
- 386 Garcia-Pineda, O., Androulidakis, Y., Le Hénaff, M., Kourafalou, V., Hole,
387 L. R., Kang, H., Staples, G., Ramirez, E., and DiPinto, L. (2020). Mea-
388 suring oil residence time with GPS-drifters, satellites, and Unmanned
389 Aerial Systems (UAS). *Marine pollution bulletin*, 150:110644.
- 390 Geuzaine, C. and Remacle, J.-F. (2009). Gmsh: A 3-d finite element mesh
391 generator with built-in pre-and post-processing facilities. *International
392 journal for numerical methods in engineering*, 79(11):1309–1331.
- 393 Harper, B., Kepert, J., and Ginger, J. (2010). *Guidelines for converting
394 between various wind averaging periods in tropical cyclone conditions*.
395 Citeseer.
- 396 Hegermiller, C. A., Warner, J. C., Olabarrieta, M., and Sherwood, C. R.
397 (2019). Wave-current interaction between Hurricane Matthew wave
398 fields and the Gulf Stream. *Journal of Physical Oceanography*,
399 49(11):2883–2900.
- 400 Hoffmeister, J. and Multer, H. (1968). Geology and origin of the Florida Keys.
401 *Geological Society of America Bulletin*, 79(11):1487–1502.
- 402 Holthuijsen, L. H., Powell, M. D., and Pietrzak, J. D. (2012). Wind and waves
403 in extreme hurricanes. *Journal of Geophysical Research: Oceans*,
404 117(C9).

- 405 Janssen, P. A. (1991). Quasi-linear theory of wind-wave generation applied
406 to wave forecasting. *Journal of physical oceanography*, 21(11):1631–
407 1642.
- 408 Johns, W. E. and Schott, F. (1987). Meandering and transport variations
409 of the Florida Current. *Journal of physical oceanography*, 17(8):1128–
410 1147.
- 411 Knaff, J. A., Sampson, C. R., and Musgrave, K. D. (2018). Statistical tropi-
412 cal cyclone wind radii prediction using climatology and persistence:
413 Updates for the western North Pacific. *Weather and Forecasting*,
414 33(4):1093–1098.
- 415 Knutson, T. R., McBride, J. L., Chan, J., Emanuel, K., Holland, G., Landsea,
416 C., Held, I., Kossin, J. P., Srivastava, A., and Sugi, M. (2010). Tropical
417 cyclones and climate change. *Nature geoscience*, 3(3):157–163.
- 418 Komen, G., Hasselmann, S., and Hasselmann, K. (1984). On the exis-
419 tence of a fully developed wind-sea spectrum. *Journal of physical*
420 *oceanography*, 14(8):1271–1285.
- 421 Kourafalou, V. H. and Kang, H. (2012). Florida Current meandering and
422 evolution of cyclonic eddies along the Florida Keys Reef Tract: Are they
423 interconnected? *Journal of Geophysical Research: Oceans*, 117(C5).
- 424 Kundu, P. K. (1976). Ekman veering observed near the ocean bottom.
425 *Journal of Physical Oceanography*, 6(2):238–242.
- 426 Landsea, C. W. and Franklin, J. L. (2013). Atlantic hurricane database un-
427 certainty and presentation of a new database format. *Monthly Weather*
428 *Review*, 141(10):3576–3592.
- 429 Lee, T. N., Leaman, K., Williams, E., Berger, T., and Atkinson, L. (1995).
430 Florida Current meanders and gyre formation in the southern Straits
431 of Florida. *Journal of Geophysical Research: Oceans*, 100(C5):8607–
432 8620.
- 433 Lee, T. N. and Mayer, D. A. (1977). Low-frequency current variability and
434 spin-off eddies along the shelf off southeast Florida. *Collected Reprints*,
435 1(1):344.

- 436 Lee, T. N. and Smith, N. (2002). Volume transport variability through the
437 Florida Keys tidal channels. *Continental Shelf Research*, 22(9):1361–
438 1377.
- 439 Lee, T. N. and Williams, E. (1988). Wind-forced transport fluctuations of the
440 Florida Current. *Journal of Physical Oceanography*, 18(7):937–946.
- 441 Li, Z. and Johns, B. (1998). A three-dimensional numerical model of surface
442 waves in the surf zone and longshore current generation over a plane
443 beach. *Estuarine, Coastal and Shelf Science*, 47(4):395–413.
- 444 Lidz, B. H. and Shinn, E. A. (1991). Paleoshorelines, reefs, and a rising sea:
445 South florida, usa. *Journal of Coastal Research*, pages 203–229.
- 446 Lin, N. and Chavas, D. (2012). On hurricane parametric wind and appli-
447 cations in storm surge modeling. *Journal of Geophysical Research: Atmospheres*, 117(D9).
- 449 Liu, Y. and Weisberg, R. H. (2012). Seasonal variability on the West Florida
450 shelf. *Progress in Oceanography*, 104:80–98.
- 451 Liu, Y., Weisberg, R. H., and Zheng, L. (2020). Impacts of hurricane Irma
452 on the circulation and transport in Florida Bay and the Charlotte Harbor
453 estuary. *Estuaries and Coasts*, 43(5):1194–1216.
- 454 Liubartseva, S., Coppini, G., Lecci, R., and Clementi, E. (2018). Tracking
455 plastics in the Mediterranean: 2D Lagrangian model. *Marine pollution
456 bulletin*, 129(1):151–162.
- 457 Longuet-Higgins, M. S. (1970). Longshore currents generated by obliquely
458 incident sea waves. *Journal of geophysical research*, 75(33):6778–
459 6789.
- 460 Longuet-Higgins, M. S. and Stewart, R. (1964). Radiation stresses in water
461 waves; a physical discussion, with applications. In *Deep sea research
462 and oceanographic abstracts*, volume 11, pages 529–562. Elsevier.
- 463 Madsen, O. S., Poon, Y.-K., and Gruber, H. C. (1989). Spectral wave
464 attenuation by bottom friction: Theory. In *Coastal Engineering 1988*,
465 pages 492–504.

- 466 Malmstadt, J., Scheitlin, K., and Elsner, J. (2009). Florida hurricanes and
467 damage costs. *southeastern geographer*, 49(2):108–131.
- 468 Marsooli, R., Lin, N., Emanuel, K., and Feng, K. (2019). Climate change
469 exacerbates hurricane flood hazards along US Atlantic and Gulf Coasts
470 in spatially varying patterns. *Nature communications*, 10(1):1–9.
- 471 Mei, C. C. (1989). *The applied dynamics of ocean surface waves*, volume 1.
472 World scientific.
- 473 Moon, I.-J., Ginis, I., Hara, T., and Thomas, B. (2007). A physics-based
474 parameterization of air–sea momentum flux at high wind speeds and
475 its impact on hurricane intensity predictions. *Monthly weather review*,
476 135(8):2869–2878.
- 477 Pinelli, J.-P., Roueche, D., Kijewski-Correa, T., Plaz, F., Prevatt, D., Zisis,
478 I., Elawady, A., Haan, F., Pei, S., Gurley, K., et al. (2018). Overview
479 of damage observed in regional construction during the passage of
480 Hurricane Irma over the State of Florida. In *Forensic Engineering 2018:*
481 *Forging Forensic Frontiers*, pages 1028–1038. American Society of
482 Civil Engineers Reston, VA.
- 483 Powell, M. D., Houston, S. H., Amat, L. R., and Morisseau-Leroy, N. (1998).
484 The HRD real-time hurricane wind analysis system. *Journal of Wind
485 Engineering and Industrial Aerodynamics*, 77:53–64.
- 486 Powell, M. D., Vickery, P. J., and Reinhold, T. A. (2003). Reduced drag coeffi-
487 cient for high wind speeds in tropical cyclones. *Nature*, 422(6929):279–
488 283.
- 489 Schott, F. A., Lee, T. N., and Zantopp, R. (1988). Variability of structure and
490 transport of the Florida Current in the period range of days to seasonal.
491 *Journal of Physical Oceanography*, 18(9):1209–1230.
- 492 Shinn, E. A. (1988). The geology of the Florida Keys. *Oceanus*, 31(1):46–53.
- 493 Siadatmousavi, S. M., Jose, F., and Stone, G. (2011). Evaluation of two WAM
494 white capping parameterizations using parallel unstructured SWAN
495 with application to the Northern Gulf of Mexico, USA. *Applied Ocean
496 Research*, 33(1):23–30.

- 497 Sikirić, M. D., Roland, A., Janeković, I., Tomazić, I., and Kuzmić, M. (2013).
498 Coupling of the Regional Ocean Modeling System (roms) and Wind
499 Wave Model. *Ocean Modelling*, 72:59–73.
- 500 Smith, N. P. (1982). Response of Florida Atlantic shelf waters to hurricane
501 David. *Journal of Geophysical Research: Oceans*, 87(C3):2007–2016.
- 502 Tolman, H. L. et al. (2009). User manual and system documentation of
503 WAVEWATCH III TM version 3.14. *Technical note, MMAB Contribution*,
504 276:220.
- 505 Van Den Bremer, T. and Breivik, Ø. (2018). Stokes drift. *Philosophical Trans-*
506 *actions of the Royal Society A: Mathematical, Physical and Engineering*
507 *Sciences*, 376(2111):20170104.
- 508 Villas Bôas, A. B., Cornuelle, B. D., Mazloff, M. R., Gille, S. T., and Arduin,
509 F. (2020). Wave–current interactions at meso-and submesoscales:
510 Insights from idealized numerical simulations. *Journal of Physical*
511 *Oceanography*, 50(12):3483–3500.
- 512 Weisberg, R., Liu, Y., and Mayer, D. (2009). Mean circulation on the west
513 Florida continental shelf observed with long-term moorings. *Geophys.*
514 *Res. Lett*, 36:L19610.
- 515 Weisberg, R. H. and Zheng, L. (2006). Hurricane storm surge simulations
516 for Tampa Bay. *Estuaries and Coasts*, 29(6):899–913.
- 517 Wu, L., Chen, C., Guo, P., Shi, M., Qi, J., and Ge, J. (2011). A FVCOM-
518 based unstructured grid wave, current, sediment transport model, I.
519 Model description and validation. *Journal of Ocean University of China*,
520 10(1):1–8.
- 521 Xian, S., Feng, K., Lin, N., Marsooli, R., Chavas, D., Chen, J., and Hatzikyri-
522 akou, A. (2018). Brief communication: Rapid assessment of damaged
523 residential buildings in the Florida Keys after Hurricane Irma. *Natural*
524 *Hazards and Earth System Sciences*, 18(7):2041–2045.
- 525 Zhang, C., Durgan, S. D., and Lagomasino, D. (2019). Modeling risk of man-
526 groves to tropical cyclones: A case study of Hurricane Irma. *Estuarine,*
527 *Coastal and Shelf Science*, 224:108–116.